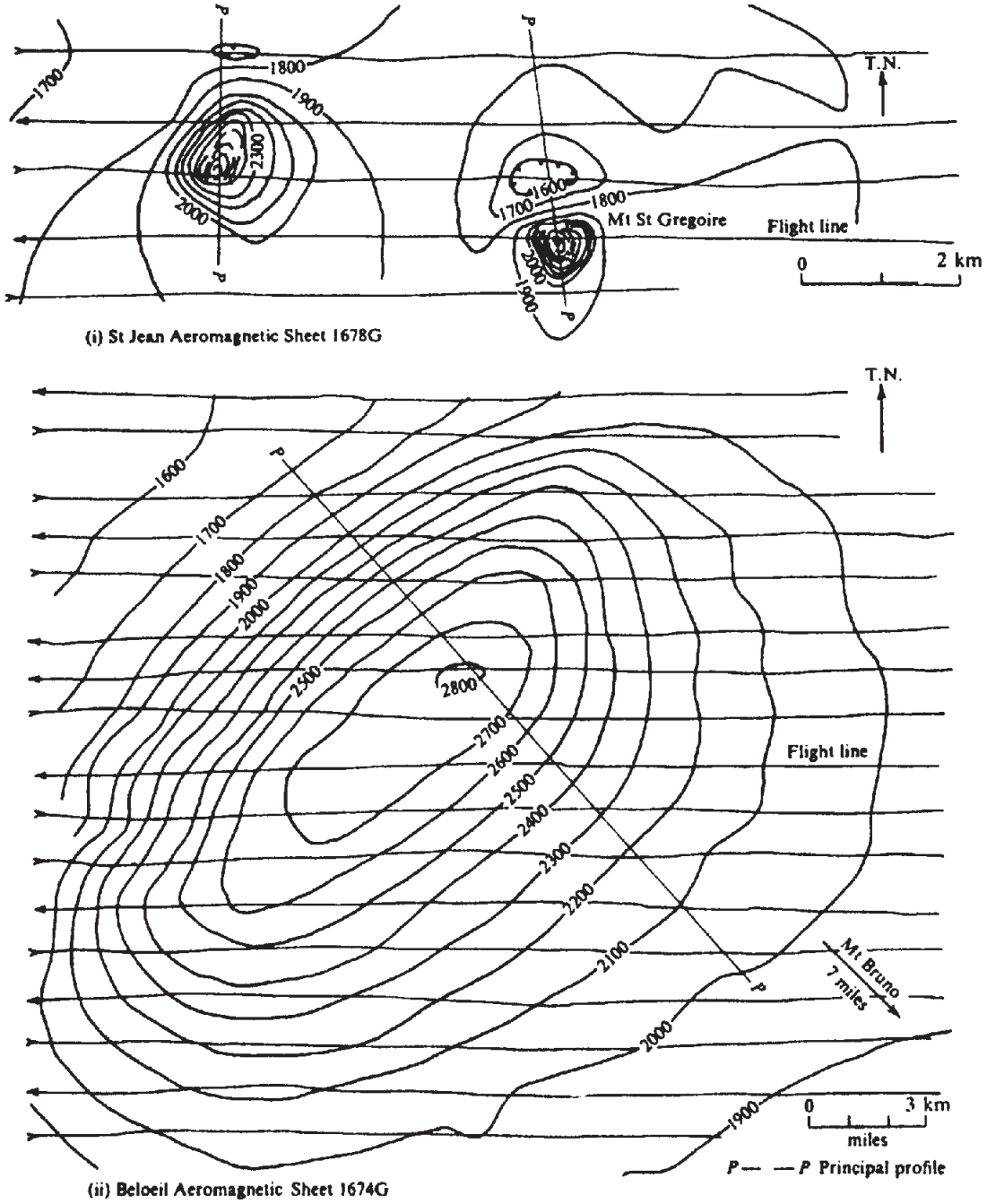

Figure 3.30. Magnetic data for three anomalous areas in the St. Lawrence lowlands. (a) Maps, C.I. = 100 nT.

3.8.2. Airborne Surveys

(1) The Monteregian hills of the St. Lawrence lowland region near Montreal were formed by igneous intrusions into sedimentary rocks. These hills are magnetic as well as topographic anomalies because of their contrast with the low susceptibility sediments. Aeromagnetic maps (Canadian Government Aeromagnetic Series, St. Jean and Beloeil) show this clearly for Mt. Bruno, Mt. St. Hilaire, Mt. Rougemont, and Mt. St. Gregoire. On the same sheets we also see two well-defined magnetic highs that are not topographic features: one about 5 km west of Mt. St. Gregoire and a larger one 11 km northwest of Mt. Bruno. One assumes that they are igneous plugs that failed to reach the eminence of the Monteregian hills.

These two features and Mt. St. Gregoire provide excellent examples of the vertical-prism model commonly employed in aeromagnetic interpretation. Figure 3.30a shows the total-field contours, whereas profiles are displayed in Figure 3.30b. Two methods

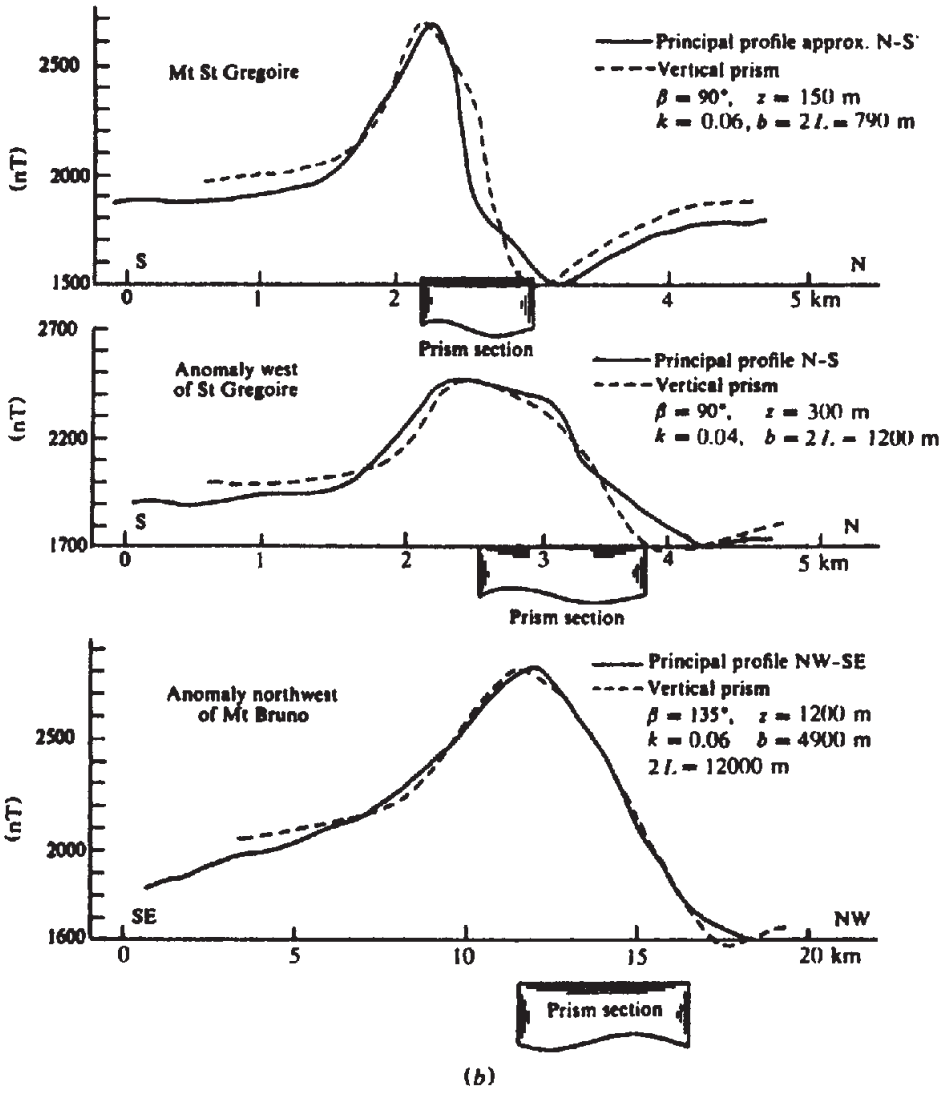

Figure 3.30. (Continued) (b) Principal profiles, $I = 60°$ and $F_e = 60\ \mu T$.

Table 3.4. *Interpretation of anomalies in the St. Lawrence lowlands.*

Anomaly	I (deg)	k (SI)	z (m)	b (m)	$2L$ (m)	Source
St. Gregoire	60	0.04	110	880	880	Vacquier (Fig. A60)
	75	0.05	110	880	670	Vacquier (Fig. A70)
	60	0.06	150	790	790	Equation (3.44c)
Anomaly near St. Gregoire	60	0.025	230	1,700	1,700	Vacquier (Fig. A60)
	75	0.03	230	1,700	1,250	Vacquier (Fig. A70)
	60	0.04	300	1,220	1,220	Equation (3.44c)
Anomaly near Bruno	75	0.08	1,130	3,660	9,140	Vacqier (Fig. A75)
	60	0.055	1,220	4,880	12,200	Equation (3.44c)

were employed to assess the magnetic characteristics. One used the models of Vacquier et al. (1951) and the other used Equation (3.44c) for a vertical prism. This allowed calculation of the susceptibility contrast k, the depth z, strike length $2L$, and width b by matching the principal profiles. The results, which fit reasonably well, are shown in Table 3.4 and in Figure 3.30b. If we assume $I = 75°$ instead of 60°, the curves have steeper slopes on the south or southeast flanks and it is necessary to increase the lateral dimensions to match the field profiles. In practical interpretations, the depth to the top of the prism is the most significant dimension. Because flight elevation was 300 m, Table 3.4 puts the St. Gregoire plug about 150–190 m above ground (Mt. St. Gregoire rises to a height of 180 m above ground). The top of

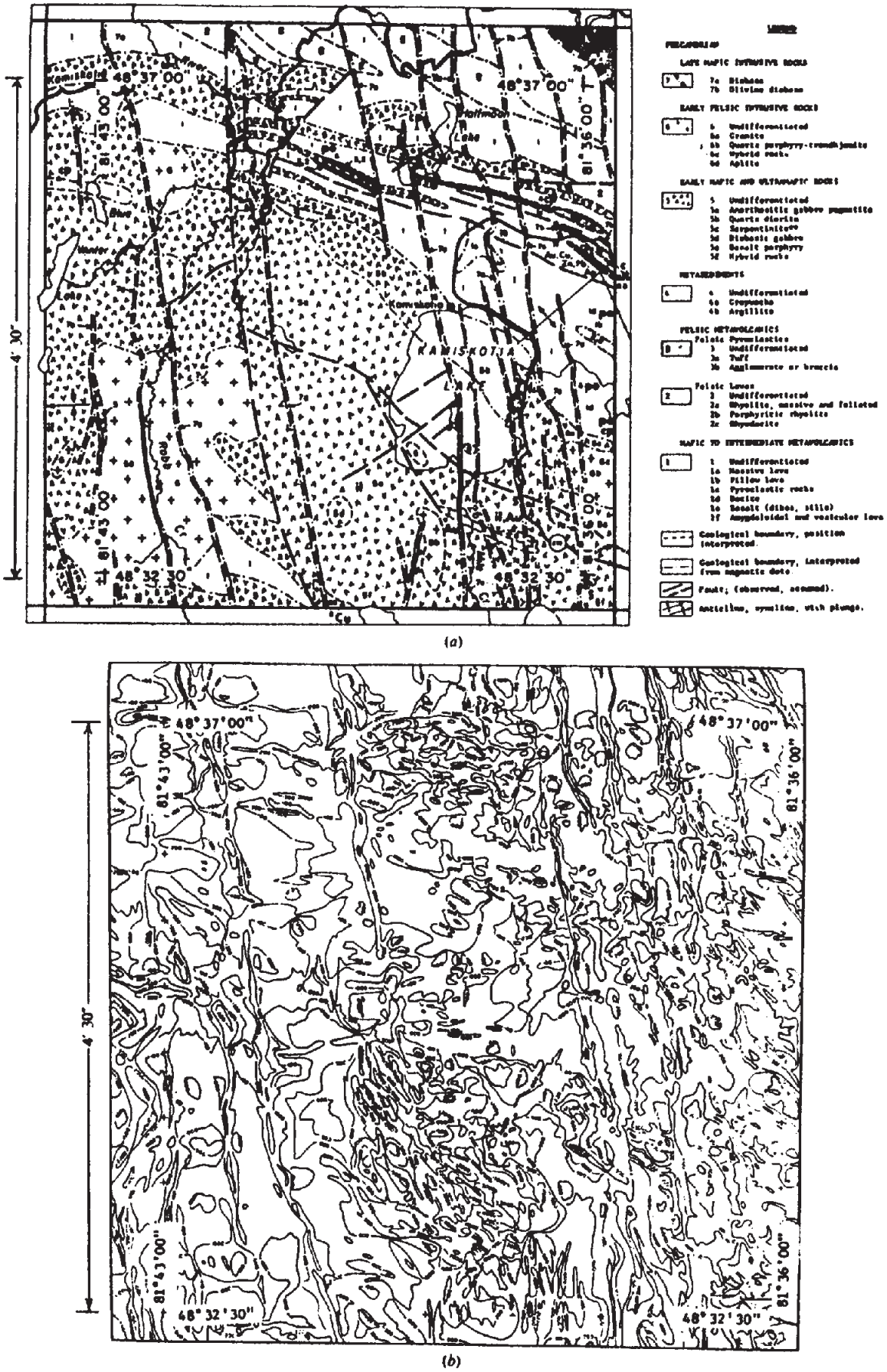

Figure 3.31. High-resolution aeromagnetic survey, Timmins area, Ontario. (From Bhattacharyya, 1971.) (a) Geological map. (b) Ground vertical-intensity map.

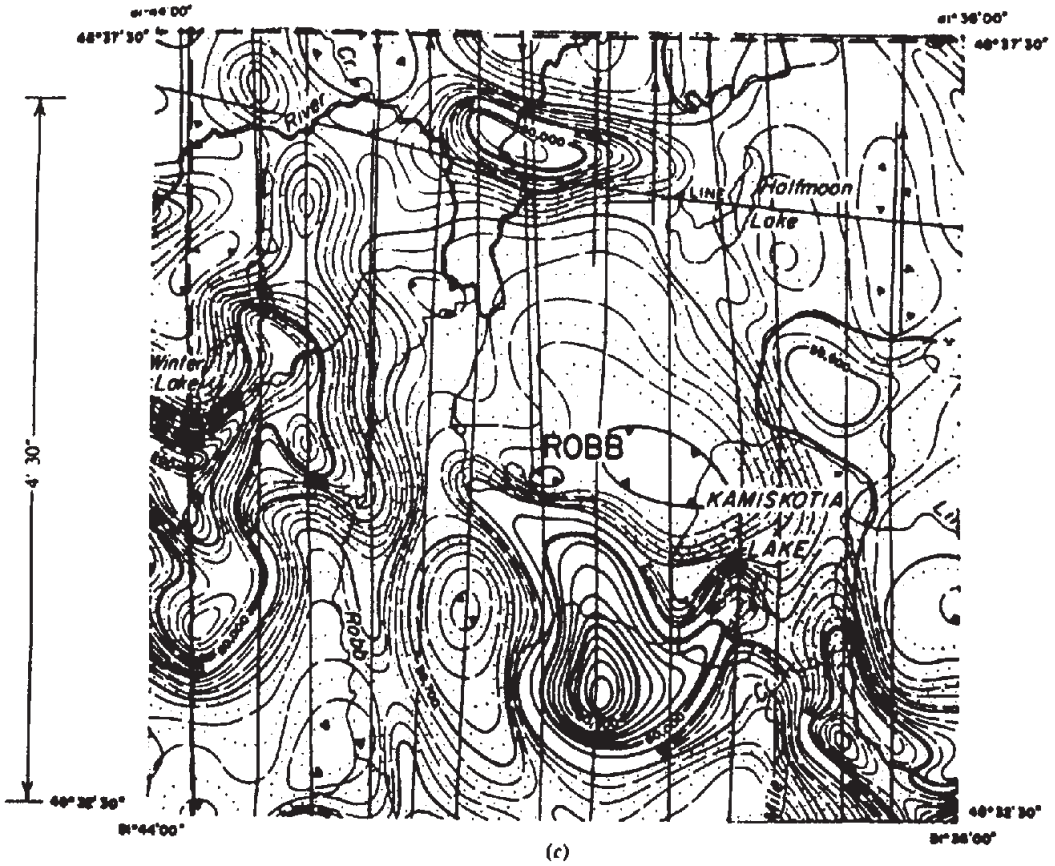

(c)

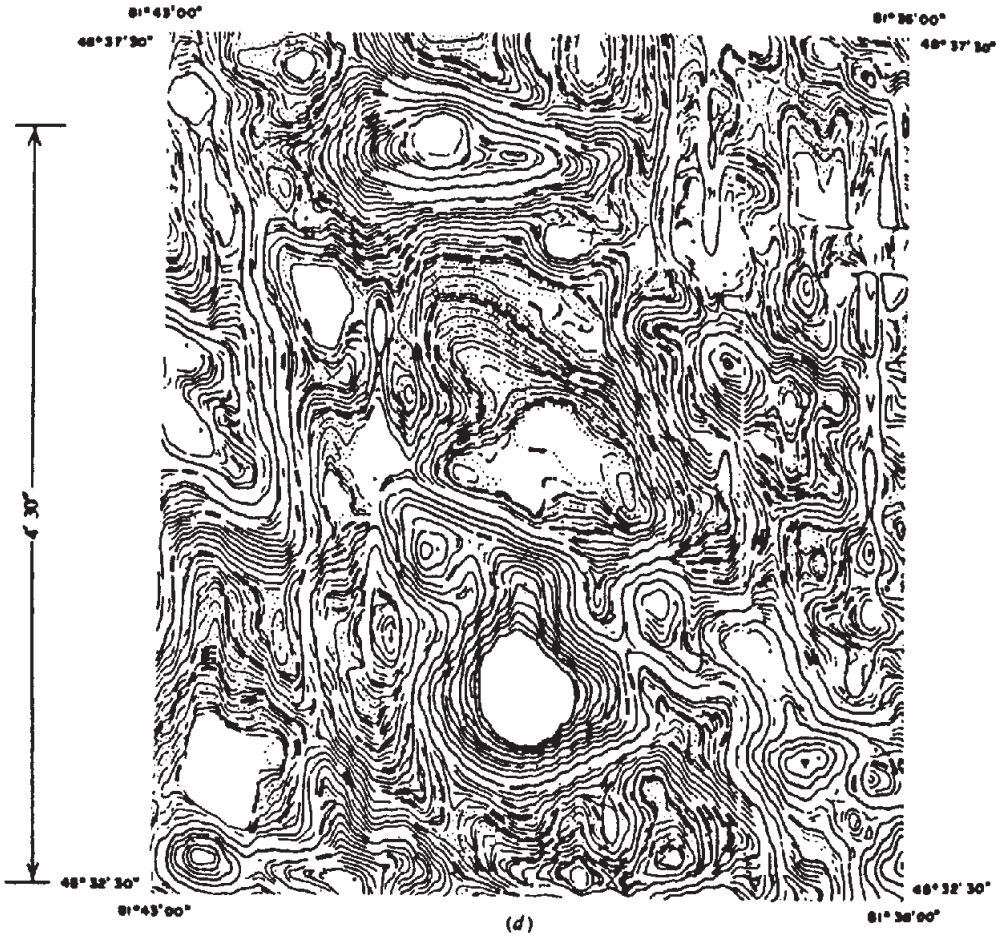

(d)

Figure 3.31. (Continued) (c) Conventional aeromagnetic map. (d) High-resolution aeromagnetic map.

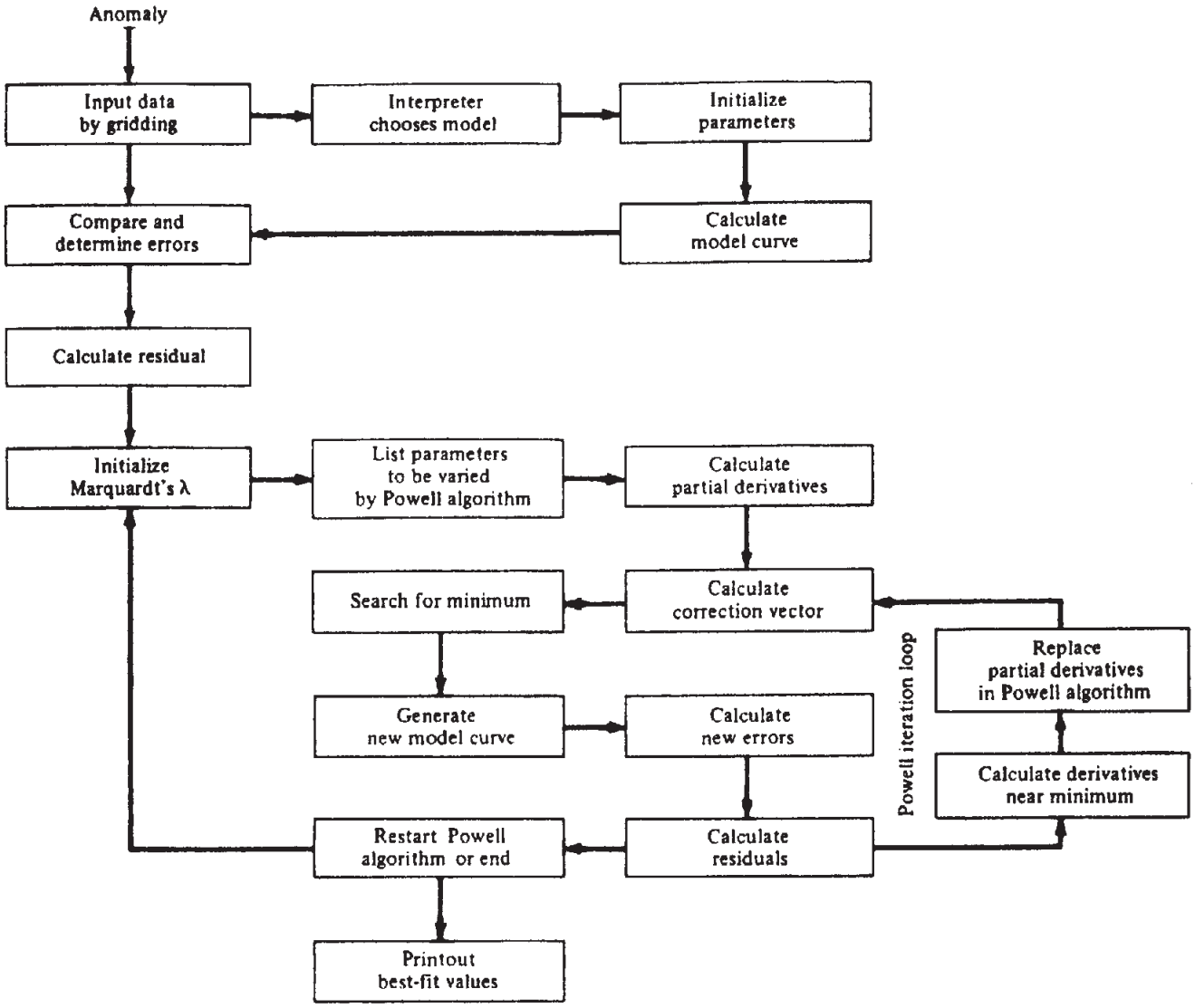

Figure 3.32. Generalized flow chart of computerized interpretation. (From McGrath and Hood, 1973.)

the anomaly near Mt. St. Gregoire is just above the surface whereas the one near Mt. Bruno is about 870 m below the surface.

(2) The use of high sensitivity aeromagnetic data has been described by Bhattacharyya (1971). In 1969, the Geological Survey of Canada arranged an experimental high-resolution survey in the Precambrian shield of northern Ontario near Timmins that used a cesium-vapor magnetometer with a sensitivity of 0.02 nT. Control of the survey was much tighter than in conventional work at the time. Line spacing was 300 m at an average altitude of 250 m and flight paths were straight within 100 m over 24 km. Double baselines perpendicular to these were flown in opposite directions every 8 km. The total field was continuously recorded at a ground station. The following were recorded on the aircraft:

1. Total magnetic field in units of 0.02 nT.
2. Total field vertical gradient in units of 0.005 nT.
3. Terrain clearance in units of 60 cm.
4. Barometric altitude in units of 3 m.
5. Doppler-radar along-track and cross distances in units of 50 m.
6. Time in seconds.

Data compilation involved the following:

1. Check of in-flight digital data and necessary corrections.
2. Calculation of coordinates.
3. Location of traverse and baseline intersections.
4. Adjustment of intersection points.
5. Calculation of, and correction for, drift.
6. Reduction of data to a common datum.
7. Reduction of corrected values for contouring.

A map of a 10 × 10 km portion of this survey is shown in Figure 3.31d.

Figure 3.31a, a provisional geological map, was prepared with help from an earlier ground vertical-

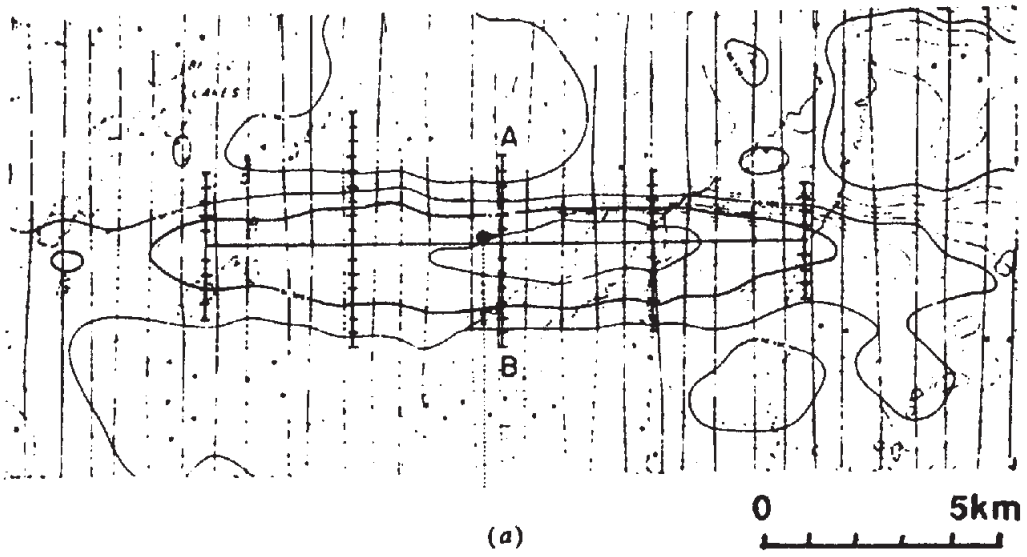

(a)

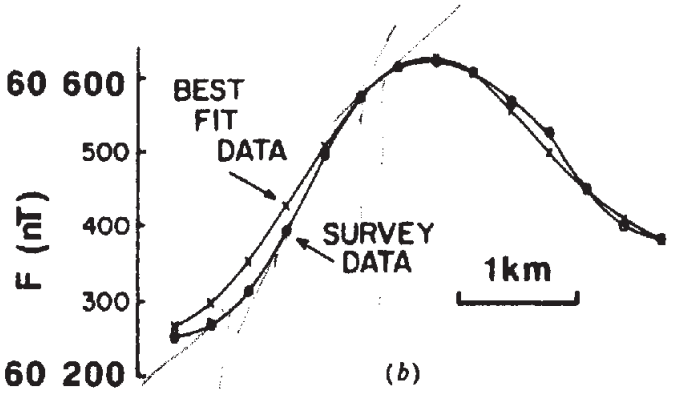

(b)

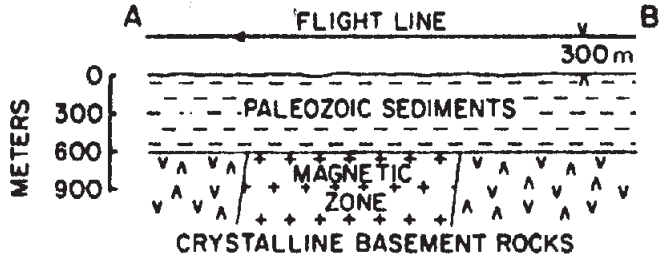

(c)

Figure 3.33. Belec Lake anomaly, Ontario. (From McGrath and Hood, 1973.) (a) Aeromagnetic map of the anomaly. (b) Profile AB and the anomaly computed from the model. (c) Inferred geological cross section.

intensity map (Fig. 3.32b). The bedrock in this area, cut by numerous N–S diabase dikes, is an Archean complex of gabbro, granite, and mafic and felsic volcanics. There are three major fault systems: The one striking N30°W is the main control for the diabase dikes, whereas the other two, trending WNW and NE, appear to have affected the dikes by shearing and deflection.

The ground survey map shows much detail, but the trends are broken up. The map from a conventional survey, Figure 3.31c, flown with a proton-precession instrument (sensitivity 0.1 nT) at 300 m with 800 m line spacing, obviously shows much less detail than the high-resolution magnetic map in Figure 3.31d. Several pronounced anomalies, probably due to gabbro, are obvious on both aeromagnetic maps, whereas the ground map does not show them clearly. The cost of the high-resolution survey was about six times greater than the conventional aeromagnetic survey, but the difference would be much less today; an equivalent ground survey on 120 m spacing would cost five to six times as much.

(3) An example of computer modeling followed the procedure diagrammed in Figure 3.32. This modeling minimizes E, the difference between observed, $D(x, y)$, and model anomalies $T(x, y)$, at m points through an iterative adjustment of n model parameters, $q_1, q_2, \ldots, q_n$:

$$E(q_1, q_2, \ldots, q_n) = \sum [D(x, y) - T(x, y, q_1, q_2, \ldots, q_n)]^2$$

The minimum of E may be found by the method of Gauss, least squares, steepest descent, or other techniques. Here it was found by a combination of the Marquart and Powell algorithms (McGrath and Hood, 1973). [See §2.7.9 for a similar gravity procedure.]

This example is of modeling a basement anomaly in the Moose River basin of the Hudson Bay lowlands in northern Ontario, which is shown in Figure 3.33. The model was a thick, steeply dipping plate. The Moose River basin contains about 600 m of nonmagnetic Paleozoic sediments overlying a Precambrian crystalline basement (based on seismic and drilling measurements). The best-fit model showed an intrabasement magnetic zone at a depth of 900 m, which corresponds to 600 m of sediment. The magnetic body is 1,730 m thick with a strike length of 14 km and dips 82° north; the susceptibility contrast is 0.029 SI, which is typical of igneous rocks. The body has its polarization vector dipping 64° with declination 107°. The local magnetic inclination is 79°, which means that the body possesses significant remanent magnetization.

Table 3.5. *Vertical-component readings in serpentine zone.*

Stn.	Z (nT)	Stn.	Z (nT)
0N	275	8N	−40
1	220	9	−10
2	224	10	−15
3	230	11	+100
4	185	12	150
5	185	13	220
6	155	14	220
7	35		

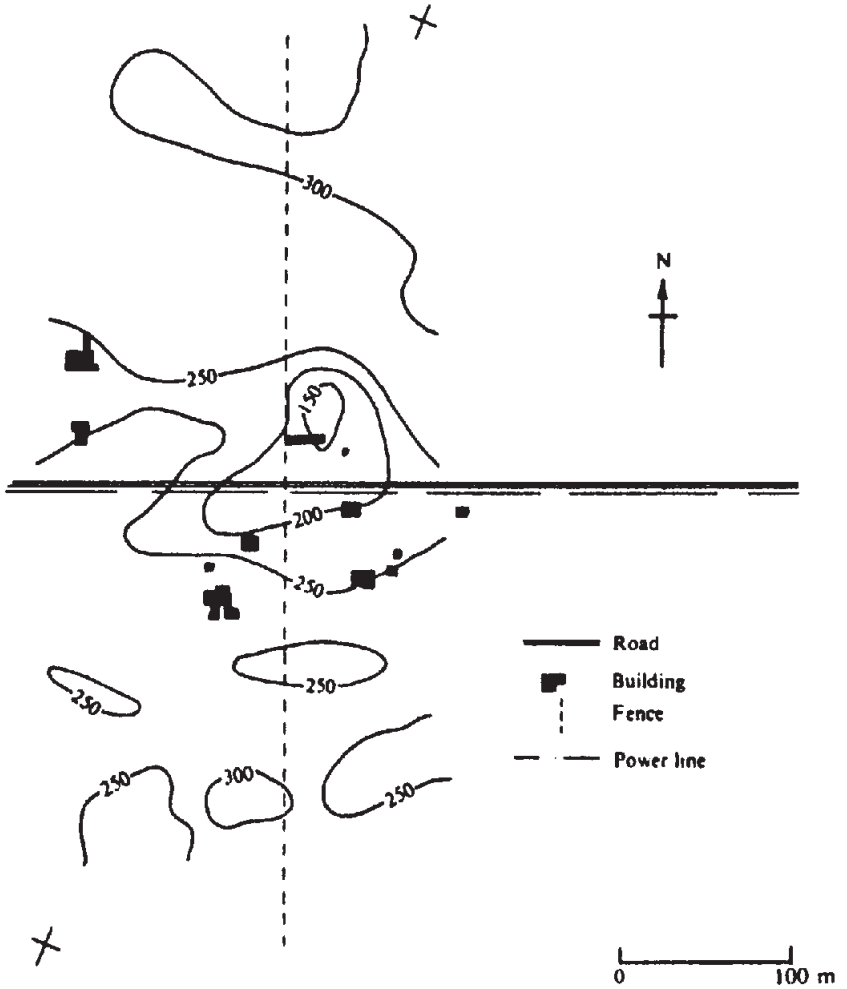

Figure 3.34. Vertical magnetic ground survey, Noranda area; C.I. = 50 nT. (After Seigel, 1957.)